







Vacuum-assisted tissue embedding for whole-heart imaging

ZHI WANG,^{1,2,†} RUIHENG XIE,^{1,†} QISHUO SHI,¹ YAFENG LI,¹  JIN CHANG,¹ JING YUAN,^{1,2}  HUI GONG,^{1,2}  AND JIANWEI CHEN^{1,2,*} 

¹*Britton Chance Center for Biomedical Photonics, Wuhan National Laboratory for Optoelectronics, MoE Key Laboratory for Biomedical Photonics, Huazhong University of Science and Technology, Wuhan, China*

²*HUST-Suzhou Institute for Brainmatics, JITRI, Suzhou, China*

[†]These authors contributed equally

*jchen1@hust.edu.cn

Abstract: The use of combined optical imaging and tissue sectioning has potential for use in visualizing heart-wide fine structures at single-cell resolution. However, existing tissue preparation methods fail to generate ultrathin cavity-containing cardiac tissue slices with minimal deformation. This study developed an efficient vacuum-assisted tissue embedding method to prepare high-filled, agarose-embedded whole-heart tissue. Utilizing optimized vacuum parameters, we achieved 94% filled whole-heart tissue with the thinnest cut slice of 5 μm . We subsequently imaged a whole mouse heart sample using vibratome-integrated fluorescence micro-optical sectioning tomography (fMOST) with a voxel size of $0.32 \mu\text{m} \times 0.32 \mu\text{m} \times 1 \mu\text{m}$. The imaging results indicated that the vacuum-assisted embedding method enabled whole-heart tissue to withstand long-term thin cutting while ensuring that slices were consistent and of high quality.

© 2023 Optica Publishing Group under the terms of the [Optica Open Access Publishing Agreement](#)

1. Introduction

The three-dimensional (3D) visualization of the entirety of a mature heart at submicron resolution is highly desired in cardiac anatomy and cardiac disease research [1]. Optical microscopy with diffraction-limited resolving power and a stage-limited imaging range is the ideal research tool for imaging fine structures across the heart [2]. However, the high optical absorption and scattering effects of cardiac tissues limit the effective imaging depth to only a few microns, hindering applications in whole-heart imaging [3,4]. To overcome this obstacle, researchers have developed tissue-clearing techniques where the complex refractive index is matched to render heart tissue transparent to optical microscopy [5,6]. Nonetheless, tissue clearing cannot fully address the problem of differences in composition among cardiac tissue, resulting in a lower imaging quality at deeper imaging depths [4,7]. In addition, dense muscular tissues limit the depth of penetration of clearing agents, and the limited penetration depth constrains the use of clearing reagents on mature hearts; therefore, researchers have primarily applied tissue-clearing techniques on embryonic hearts [8].

Another strategy for whole-heart imaging is based on both optical imaging and tissue sectioning to extend the imaging depth limit. This strategy includes fluorescence micro-optical sectioning tomography (fMOST) [9,10] and knife-edge scanning microscopy [11]. These technologies require tissues to be embedded in plastic media, such as resin or paraffin, which provide physical support and enhanced stiffness for thin tissue sectioning. However, the dehydration of tissues in the embedding process may severely shrink cavity-containing cardiac tissues, distorting the fine structures [12]. In addition, the sample preparation cycle of the plastic embedding method lasts from a few days to weeks. To remedy these disadvantages, researchers have employed highly efficient cryofixation and embedding to preserve the original shape of cardiac tissue. However,

the cryogenic environment hinders the use of high numerical aperture (NA) objectives with short working distances, impeding high-resolution imaging [13,14]. Recent studies have reported that cryo-fMOST enables imaging of the whole heart with submicron resolution [15]; this technology is expected to have applications in the field of spatial multiomics. However, this complex system comprises a cryogenic module with an extra cascade and a heat insulation device. Therefore, the development of a highly efficient tissue preparation method that enables serial thin cutting of the intact heart and preserves its original morphology at room temperature is required.

One potential solution is the use of agarose for cardiac tissue embedding. Because the agarose-embedding preparation process does not involve dehydration, the original morphology of the tissue is maintained [16]. Researchers have widely employed agarose embedding for parenchymal organs, such as the brain and the liver, combined with vibratome sectioning to generate sections of thickness from 4 μm to 1 mm [17]. However, few studies have used this method for other cavity and tubular organs. We hypothesized that this is because agarose is a macromolecular elastic material. Therefore, it cannot penetrate body cavity and tubular tissues through intercellular spaces; instead, it enters the tissues through communicating vessels such as the arteries. Specifically, low-concentration agarose (1%–3%) with a low viscosity [18] can flow in and fill cavities spontaneously, but it deforms easily during the sectioning process due to its low intrinsic stiffness, failing to produce sections thinner than 20 μm . In contrast to low-concentration agarose, high-concentration agarose (4%–6%) provides sufficient mechanical strength for tissue sectioning, but it cannot pass through the communicating vessels easily due to its high viscosity. Although direct injection can facilitate the agarose filling procedure, the agarose may trap air in the heart cavity and form bubbles during the curing process [19]. Therefore, this study developed a vacuum-assisted embedding method that was incorporated into the heart tissue preparation and vibratome sectioning processes. This method enables room-temperature whole-heart imaging at single-cell resolution with minimal distortion.

We developed a vacuum-assisted tissue embedding technique for preparing a whole-heart sample that employed a high-filled agarose medium and an advanced mechanical cutting method. This quantitative study implemented tissue sectioning and imaging experiments to examine how vacuum parameters and agarose concentration affect tissue embedding quality. An agarose-embedded heart was prepared according to a set of optimized parameters and imaged using a vibratome-integrated fMOST system; the results demonstrated that the tissue withstood ultrathin serial sectioning and was compatible with whole-organ 3D high-resolution imaging applications.

2. Materials and methods

2.1. Animals

This study used thirty-one 8- to 12-week-old C57BL/6J male mice (Jackson Laboratory, Bar Harbor, ME, USA). The mice were kept in a 12-h light/dark cycle with food and water provided ad libitum. All animal experiments were performed according to procedures approved by the Institutional Animal Ethics Committee of Huazhong University of Science and Technology.

2.2. Tissue preparation for whole-heart imaging

A schematic of the proposed vacuum-assisted tissue preparation procedure for whole-heart imaging is presented in Fig. 1(a). The procedure contained the following three primary steps: tissue dissection, vacuum-assisted embedding, and whole-organ imaging.

In the tissue dissection stage, the mice were anesthetized with a 1% sodium pentobarbital solution and subsequently intracardially perfused with 0.01 M PBS (Sigma-Aldrich, USA), followed by 4% PFA (Sigma-Aldrich, USA) in 0.01 M PBS. The hearts were then excised and post-fixed in 4% PFA at 4 °C for 24 h. Subsequently, each heart was rinsed overnight at 4 °C in 0.01 M PBS and prepared for embedding.

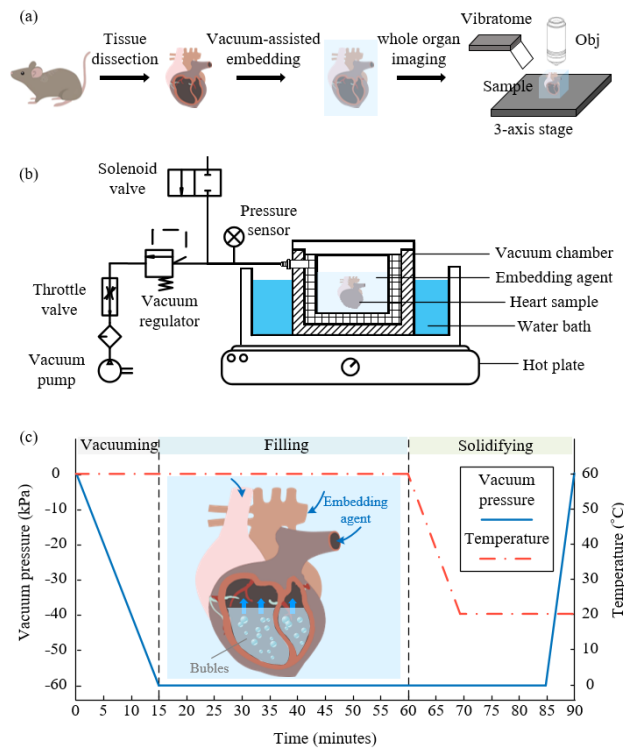


Fig. 1. Preparation of cardiac tissue for whole-heart imaging. (a) Procedure for preparing whole-heart tissue with vacuum embedding method and imaging with vibratome-integrated fMOST. (b) Vacuum-assisted elastic embedding apparatus. (c) Vacuum-assisted whole-heart sample embedding process.

To create the embedding medium in the tissue embedding stage, oxidized agarose was prepared by adding agarose Type I-B (Sigma-Aldrich, USA) to a 10 mM NaIO_4 (Sigma-Aldrich, USA) solution and stirring for 2–3 h in room temperature without exposure to sunlight. The solution was repeatedly washed and resuspended in PBS to increase the final concentration to 4.0–6.0 wt%. The whole-heart tissue was then placed in a custom-built vacuum-assisted tissue embedding system filled with agarose solution, and the embedding process proceeded automatically (Detailed description is in Section 2.3).

In the whole-organ imaging stage, the vibratome-integrated fMOST system was implemented to image the whole-heart sample. First, optical microscopy was used to perform in situ imaging to acquire the superficial layer information of the sample. Subsequently, we employed the vibratome to remove the imaged layer; this process was repeated until the entire heart sample was imaged. A three-axis linear stage was used to move and align the sample between the vibratome and the microscope for alternated sectioning and imaging (the vibratome-integrated fMOST are detailed in Section 2.5).

2.3. Vacuum-assisted tissue embedding

Figure 1(b) presents a schematic of the vacuum-assisted tissue embedding system, which was designed to automate the tissue embedding process with an improved filling effect. The system was composed of a custom-built vacuum chamber and a pressure control module. The whole-heart tissue was placed in the vacuum chamber and immersed in an embedding agent (i.e., agarose solution). The vacuum chamber was placed in a water bath heated by a hot plate.

The vacuum chamber had a double-layer structure. The inner bladder (the hatched part of the grid pattern) was a detachable silicone mold and was easily separated from the prepared sample in the demolding operation. The outer shell (the hatched part of the diagonal pattern) was made of aluminum alloy with a high heat transfer coefficient of $155 \text{ W}/(\text{m}\cdot\text{K})$; this facilitated the heat transfer from the water bath to the embedding agent and the maintenance of the embedding agent molten state. The acrylic cover of the vacuum chamber served as an observation window.

The pressure control module was composed of a vacuum line and an atmospheric line. A vacuum pump, a vacuum regulator, a throttle valve, and a pressure sensor were connected to the vacuum chamber, forming the vacuum line. The vacuum regulator controlled the vacuum pressure, the throttle valve adjusted the vacuum speed, and the pressure sensor monitored the pressure changes in the vacuum chamber. A solenoid valve connected to the vacuum chamber to form the atmospheric line allowed air to enter when the vacuum was lifted.

Figure 1(c) illustrates the vacuum-assisted tissue embedding process, which can be divided into the following three steps: (1) vacuuming, (2) filling, and (3) solidifying. In the vacuuming step, the hot plate maintained a constant water temperature (60°C). One or more hearts were pat-dried and placed in the inner bladder of the vacuum chamber filled with melted oxidized agarose. Then, the vacuum pump and the vacuum regulator were turned on to adjust the chamber to a low-pressure state (i.e., -60 kPa). The vacuum speed was set at $5\text{--}10 \text{ kPa}/\text{min}$ to avoid rapid pressure changes that could cause rigid shocks to the soft cardiac tissues. The vacuum pressure and the bath temperature remained constant during the filling process; the agarose automatically filled and fully cross-linked the inner cavities of the heart. In the solidifying step, the hot plate was turned off and the temperature of the vacuum chamber cooled naturally to room temperature (i.e., 20°C) for approximately 0.5 h to solidify the embedding agent. Subsequently, the vacuum pump and the vacuum regulator were turned off, the solenoid valve was turned on, and the agarose-embedded organs were separated from the silicone mold and stored in PBS at 4°C .

2.4. Vibratome sectioning and analysis

To investigate the filling effect and cutting performance of the vacuum-assisted embedding method, we used a commercial vibratome (VT1200S, Leica, Germany) to cut the agarose-embedded whole-heart sample and quantitatively analyzed two key metrics, namely, the fill factor (F) and the thinnest slice thickness (T). F is defined as the proportion of filled agarose in the heart cavity; a high F provides more adequate support for cardiac tissue. T is defined as the thickness of the thinnest intact section obtained. A lower T represents a better stiffness-enhancing effect of agarose embedding on cardiac tissue. To measure the T , we cut the tissue starting from $20 \mu\text{m}$ and decreased by $1\text{-}\mu\text{m}$ increments until reaching the thinnest complete slice. The fMOST system was used to image all slices to verify completeness.

The fill factor of a whole-heart sample was obtained through a multistep process. First, the prepared sample was cut to a thickness of $200 \mu\text{m}$, and all slices were manually collected and placed on slides. A total of $20\text{--}30$ cardiac slices were cut and collected for a whole-heart sample depending on its size. Subsequently, a light microscope (IX73, Olympus, Japan) was used to image the serial slices. The images were imported into Amira software (version 6.1.1, FEI, Mérégnac Cedex, France); the agarose-filled areas and the hollow areas were semi-automatically segmented using the watershed algorithm and manual correction. Figure 2 presents an example of the fill factor calculation of a given heart, where the vacuum pressure was set at -80 kPa and the vacuum time was set at 30 minutes. Figure 2(a) is the original image of the selected slice in Fig. 2(c); Fig. 2(b) is colored using the watershed algorithm, where the blue indicates the agarose-filled area and the red indicates the hollow area. A total of 25 slices were collected and imaged, and the F of each slice is listed on the top right of each image [Fig. 2(c)]. The red framed image refers to the example in Figs. 2(a) and 2(b), which have a fill factor of 0.97. The total F is the average of the 25 slices, which was 0.95 in this example.

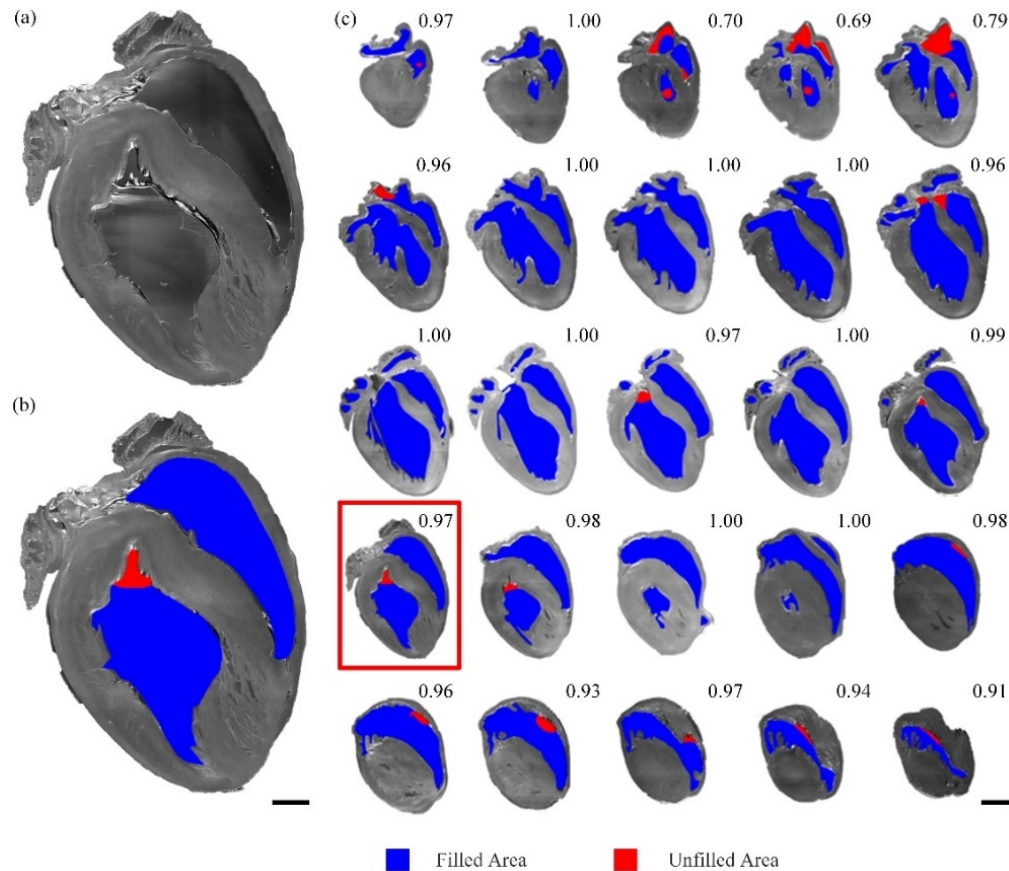


Fig. 2. Quantitative analysis of agarose filling effect in one experiment where the vacuum pressure was set at -80 kPa and the vacuum time was set at 30 minutes. (a) An original slice. (b) Defined filled and hollow areas using the watershed algorithm. (c) Calculation of fill factor for each slice, the fill factor is listed at the top right of each figure. The red framed image refers to the example in (b). Scale bars: (a–b) 1 mm, (c) 2 mm.

2.5. Vibratome-integrated fMOST

The vibratome-integrated fMOST system was composed of a line-illumination modulation (LiMo) microscope, a precision vibratome, and a three-axis linear stage. Our previous paper described the custom-made LiMo microscope in detail [20]. In brief, the illumination was generated by an expanded and reshaped laser beam (Cobolt Jive, 561 nm, 100 mW, Hübner Photonics, Germany), which was relayed to the focal plane of the objective (XLUMPLFLN 20×, NA 1.0, Olympus, Japan) to generate line illumination. The excited fluorescence signal was isolated by a long-pass filter (ET590lp, Chroma, USA) and recorded by a scientific complementary metal-oxide-semiconductor camera (ORCA-Flash 4.0, Hamamatsu, Japan) in subarray mode at the maximum frame rate. The LiMo microscope acquired images at a voxel resolution of $0.32\ \mu\text{m} \times 0.32\ \mu\text{m} \times 1\ \mu\text{m}$. The LiMo microscope imaged a shallow layer of an 8- μm -thick tissue for each sample; back-and-forth line scanning was then used to image a 666- μm -wide, 7.4-mm-length, 1- μm -thick strip stack. The largest axial plane of the heart sample in our experiment is about 6.3 mm \times 7.4 mm, 10 strips were formed and spliced in each axial plane imaging to cover the whole heart sample. Our previous paper also described the characteristics

of the custom-built precision vibratome, which was composed of a vibrating driver, a DP–DP flexure, and a ceramic blade [17]. The DP–DP flexure was designed to simultaneously achieve a high vibration frequency and to suppress parasitic motion. The vibratome used in this study operated at a frequency of 180 Hz with motion errors of less than 250 nm. We set a cutting thickness of 8 μm in the whole-heart imaging experiment.

3. Results and discussion

3.1. Optimization of the vacuum parameters

Agarose filling can effectively protect the suspension and cavity structure of cardiac tissue. To obtain a high F for an agarose-embedded whole-heart sample, optimizing the vacuum embedding parameters of vacuum pressure (p) and vacuum time (t) is essential. We devised a set of experiments to study the influence of the vacuum parameters on the filling effect of agarose.

In the first experiment the concentration of the agarose (c) was set at 5%, t was set to 30 minutes, and p was varied from 0 kPa to -80 kPa with increments of 20 kPa. Each experiment was repeated three times with similar results. Figure 3(a) presents the F of whole-heart samples under various vacuum pressures. The results demonstrated that the F increased as the vacuum pressure increased. The F reached the highest value (0.95) when $p = -80$ kPa. However, we observed that the agarose solution boiled and formed large bubbles when $p = -80$ kPa. This occurred because the agarose solution contained water, and the boiling point of water at -80 kPa is 60 °C [21]. To maintain the molten state of agarose during the filling process, the temperature of the water bath must be higher than 60 °C, which causes the agarose solution to boil. Therefore, we could avoid this phenomenon by adjusting the vacuum pressure to -60 kPa.

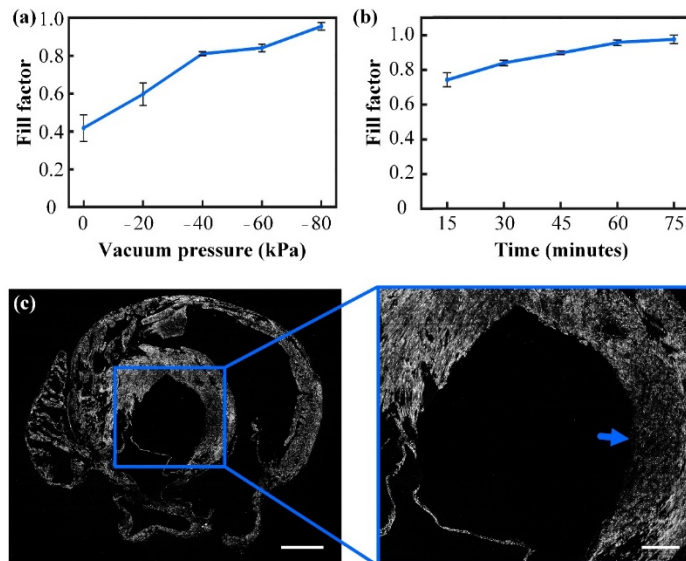


Fig. 3. Influence of experimental parameters on filling effect and cutting quality. (a) Vacuum pressure as a function of the fill factor of whole-heart samples, where the vacuum time was fixed at 30 minutes. ($n = 3$ for each experiment) (b) Vacuum time as a function of the fill factor of whole-heart samples, where the vacuum pressure was fixed at -60 kPa. ($n = 3$ for each experiment) (c) Microscopic optical image of a selected heart section containing cavities not fully filled with agarose. Scale bars: 1 mm (left), 300 μm (right).

In the second experiment, we studied the influence of vacuum time on the filling effect. In this experiment, c was set at 5%, p was set to -60 kPa, and t was varied from 15 to 90 minutes at

15-minute increments. Each experiment was repeated three times with similar results. Figure 3(b) presents the F of the whole heart versus the t . The results revealed that F increased with t up until $t > 60$ minutes, at which point F only increased slightly [e.g., 0.94 at 60 minutes vs. 0.95 at 90 minutes]. Therefore, we recommend a t value of 60 minutes for reasons of time efficiency.

Further detailed analysis of all the experimental results revealed that the unfilled areas (i.e., air bubbles) were mostly distributed at the borders of the atria and ventricles. This phenomenon can also be seen in Fig. 2. During the filling process, these bubbles contact both heart tissue and agarose solution interfaces. According to force analysis, these bubbles suffered both friction of the tissue surface and the tension of the agarose solution at the same time, making them difficult to be expelled. However, despite containing incompletely filled cavities, the tissue still can be cut intact, and one example is shown in Fig. 3(c). This is a microscopic image of a selected section of heart tissue with an incompletely filled cavity. The left figure shows the complete cut surface without any visible defects. The complete cutting is possible because the outer fully-wrapped agarose and the inner partially-filled agarose still provide sufficient physical support for the heart tissue. But a decrease in cutting quality can be observed from the tissue near the unfilled area in the enlarged figure on the right, as indicated by the blue arrow. This is due to the lack of support leading to local stiffness weakening, which in turn leads to a decrease in the ability of local tissues to resist deformation caused by cutting forces. Thus, vacuum-assisted embedding enables the heart to withstand continuous ultrathin cutting even if the local cavity is not fully filled. However, in order to ensure the quality of 3D microscopic imaging of whole heart sample, it is necessary to ensure as high a fill factor as possible, so as to reduce local image quality degradation. Based on this criterion and the above experiments, the optimized vacuum parameters are -60 kPa vacuum pressure and 60 minutes vacuum time.

Using the optimized vacuum parameters, we also conducted a vacuum-assisted embedding experiment on the hearts of an 18-week-old male mouse and an 18-week-old female mouse, and the results are shown in Fig. S1 (Supplement 1). The results show that the filling factors of the two experiments are all above 0.93, which proves the vacuum-assisted tissue embedding method can be broadly applied to other cardiac samples with different biological variables such as age and sex.

3.2. Determination of the agarose concentration

In addition to analyzing the fill factor, we also analyzed the cutting performance of the tissue. A smaller T represents better cutting performance. T is highly associated with the mechanical properties of the embedding medium (i.e., the stiffness), which enable the elastic tissues to resist deformation caused by the cutting force. The stiffness of the embedding medium is primarily determined by the agarose concentration. In the third experiment we used the vibratome to cut the 4%, 5%, and 6% agarose-embedded whole-heart samples in the sagittal/ coronal plane and measured the corresponding T . The p and t were set at -60 Kpa and 60 minutes. The results are presented in Fig. 4; the cutting thickness is listed on the top left of each graph. We cut 4% agarose-embedded heart tissue with a thickness of 16, 15, and 14 μm , respectively [Fig. 4(a)]. All slices were collected and imaged using the LiMo microscope. Although the 16- and 15- μm slices were complete and free from obvious defects, we discovered breakage on the 14- μm slice, as indicated by the blue arrows. Thus, T was 15 μm when $c = 4\%$. Similarly, we concluded that T was 9 μm when $c = 5\%$ [Fig. 4(b)] and T was 5 μm when $c = 6\%$ [Fig. 4(c)]. Since the orientation of myocardial fibers is anisotropic, we also performed the thinnest slice cutting test along the axial plane, and the results are shown in the Fig. S2 (Supplement 1). The results indicated that different cut section or myocardial fiber direction had no significant effect on the thinnest cutting thickness.

These thin slices were difficult to collect manually due to their delicate nature. Therefore, the measured T value may be larger than the true value. However, the experimental results

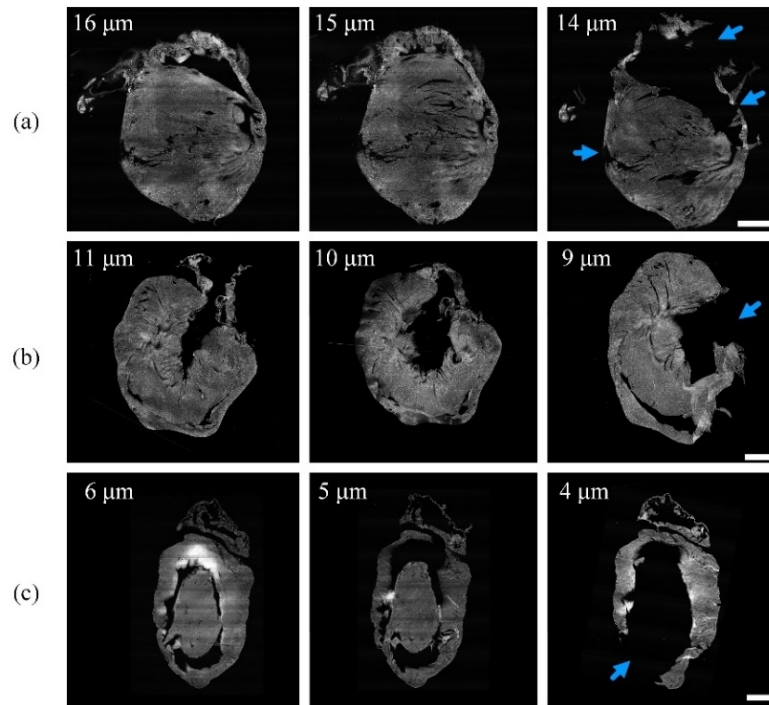


Fig. 4. Cutting the agarose-embedded whole-heart tissue along the sagittal/coronal plane with a concentration of (a) 4%, (b) 5%, and (c) 6%, respectively; arrows indicate the location of tissue breakage. Scale bars: 1 mm.

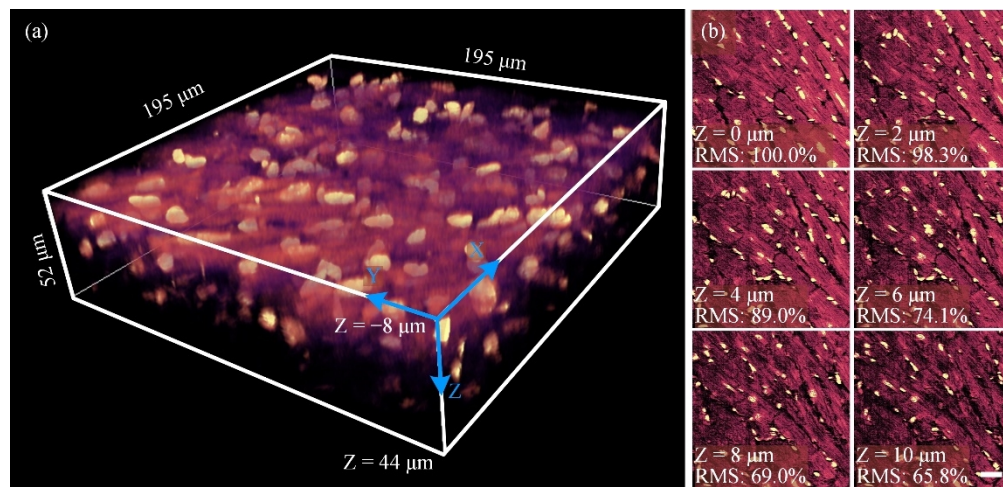


Fig. 5. Effective imaging depth measurement. (a) LiMo imaging of heart tissue at a depth of 52 μm from $Z = -8 \mu\text{m}$ to $Z = 44 \mu\text{m}$ with a Z increment of 1 μm . (b) $Z = 0$ at the top surface of the sample; scale bar: 20 μm .

demonstrated that a higher concentration of agarose resulted in a thinner T . A higher concentration of agarose results in a stiffer embedding medium; however, it may also increase the viscosity of the agarose reagent, making it difficult to fill in the cavities. Crucially, excessive stiffness increases brittleness and reduces plasticity, resulting in increased chatter marks on the cutting surface. Therefore, we recommended a concentration of 6% for thin-slice cutting.

3.3. Vacuum-assisted embedding for whole-heart imaging

For axial continuous data acquisition, we first evaluated the maximum imaging depth of each cycle, which helped determine the cutting thickness. The maximum imaging depth was measured using imaging of propidium iodide (PI)-stained mouse heart tissue with the LiMo microscope. We defined the top surface of the tissue as $Z = 0$ and imaged the sample from above the tissue surface ($Z = -8\ \mu\text{m}$) to below the surface ($Z = 44\ \mu\text{m}$) with a scanning increment of $1\ \mu\text{m}$ (Fig. 5). We employed the root mean square (RMS) of image intensity to quantitatively evaluate the image quality [22]. The brightness and contrast of the image reached the maximum at the top surface ($Z = 0\ \mu\text{m}$) and continued to decline as the imaging depth increased. The RMS values from top left to bottom right are 4197 (100%), 4125 (98.3%), 3737 (89.0%), 3110 (74.1%), 2896 (69.0%), and 2763 (65.8%) respectively. To ensure the imaging quality, we allowed an approximately 30% RMS drop in this imaging sequence [23]. Based on this criterion, we identified $8\ \mu\text{m}$ as the maximum imaging depth due to its RMS of 2896. Thus, our system has a preferred tissue cutting thickness of $8\ \mu\text{m}$ for 3D continuous imaging of a PI-stained whole mouse heart.

It is worth noting that absorption/scattering coefficients of cardiac tissue have local peaks at both $\sim 450\ \text{nm}$ and $\sim 550\ \text{nm}$ [24], the imaging depth will be slightly reduced if the fluorophore falls within this range. We have also tested TRITC-dextran (excitation/emission: $561\ \text{nm}/591\ \text{nm}$) and DAPI (excitation/emission: $358\ \text{nm}/461\ \text{nm}$) fluorophores labeled agar-embedded heart slices respectively, and the corresponding imaging depths were $8\ \mu\text{m}$ and $6\ \mu\text{m}$ [Fig. S3 in Supplement 1]. The excited fluorescence signal was isolated by two filters, ET570lp and ET450/50 m (Chroma, USA), respectively. The imaging depth of DAPI is slightly decreased. Considering that our thinnest slice thickness is $5\ \mu\text{m}$ [Fig. 4(c)], it can fully cover the limited imaging depth.

Subsequently, we employed the vibratome-integrated fMOST to image an agarose-embedded whole-heart sample at a voxel resolution of $0.32\ \mu\text{m} \times 0.32\ \mu\text{m} \times 1\ \mu\text{m}$. The heart tissue was embedded with 6% agarose using the vacuum embedding method with a vacuum pressure of $-60\ \text{kPa}$ for 60 minutes. The whole-heart sample was immersed in a PI solution, and the cardiac cells were counterstained automatically during the imaging process. A total of 930 slices were cut at a thickness of $8\ \mu\text{m}$, and LiMo microscopy was used to image 7440 axial sections. The total data acquisition time was approximately 30 h, and the entire dataset size was approximately 7.5 TB. The 3D rendering of the whole heart with a size of approximately $7.4\ \text{mm} \times 6.3\ \text{mm} \times 7.4\ \text{mm}$ is displayed in Fig. 6(a). The suspended papillary muscle structures are indicated by a blue arrow; the hollow ventricles were well-preserved, indicating that the high-filled agarose medium provided adequate physical support. Figure 6(b) illustrates the axial images with an increment of $1.0\ \text{mm}$. The PI-stained results indicated that the vacuum embedding method enabled the heart tissue to withstand consistent vibratome cutting, resulting in an ultra-smooth cutting surface for submicron-resolution precision imaging. Figure 6(c) presents a region on the ventricular wall with three groups of uniquely oriented cardiomyocytes; both the epicardial and endocardial fibers were oriented vertically (dotted cross-section), whereas the intermediate fibers were oriented horizontally (striped cross-section). These results agreed with those of another study [25], and the distinct cross-sectional characteristics served to roughly delineate the borders of the epicardium (Epi), myocardium (Myo), and endocardium (Edo) of the ventricular wall, respectively [white dotted line in Fig. 6(c)]. The enlarged cardiomyocytes are indicated by the white rectangle in Fig. 6(c); this demonstrates the excellent cutting quality enabled by vacuum embedding. Furthermore, the submicron resolution of fMOST allowed for the sarcomeres to

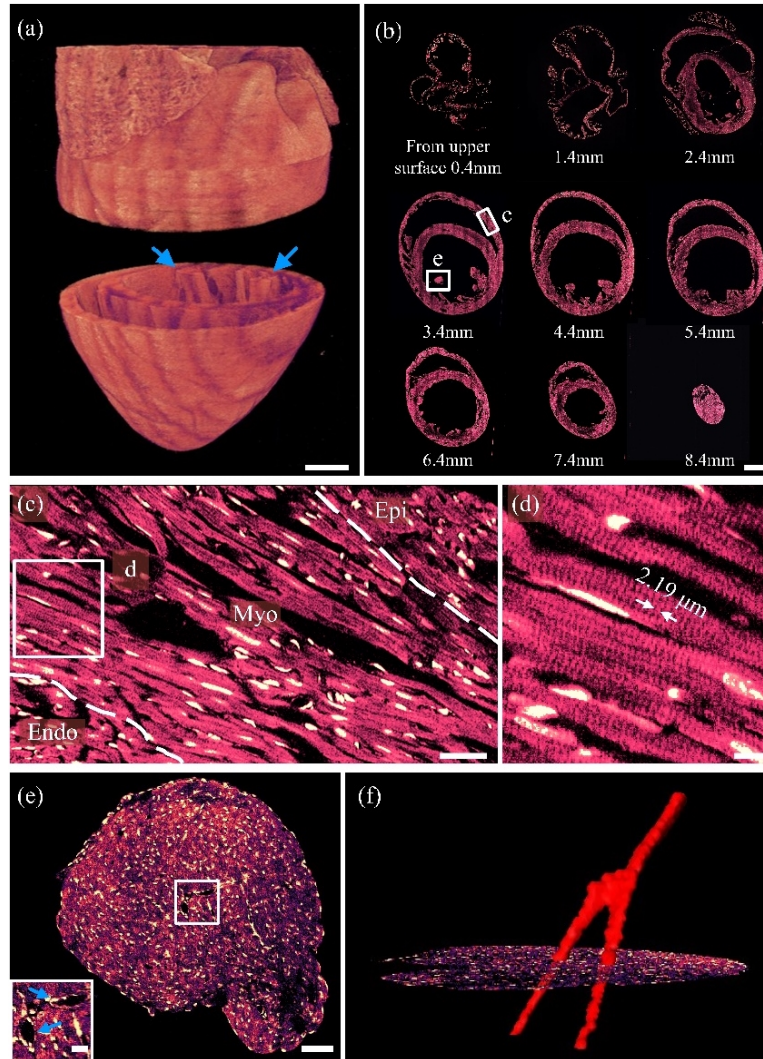


Fig. 6. Imaging of a whole mature mouse heart using vibratome-integrated fMOST. (a) 3D rendering of the whole heart. (b) Sequential axial images at equal intervals of 1.0 mm. (c) Enlarged view of the corresponding white rectangle in (b), displaying the cardiac cells of the ventricular wall. Epi: epicardium; Myo: myocardium; Endo: endocardium. (d) Enlarged view of the corresponding white rectangle in (c), one of the sarcomeres was measured and the period was 2.19 μm. (e) Enlarged view of the corresponding white rectangle in (b), which is the cross-section of a papillary muscle, and an inset of the enlarged segment of blood vessels, which corresponds to the white rectangle in the main image. (f) Enlarged view of partially reconstructed blood vessels at the starting position of the tracing in (e). Scale bars: (a) 1 mm, (b) 1 mm, (c) 50 μm, (d) 10 μm, (e) 50 μm; inset graph 10 μm.

be distinguished with a period of $2.19\ \mu\text{m}$, as illustrated in Fig. 6(d); studies have commonly observed sarcomeres with electron microscopy [26].

Figure 6(e) presents an enlargement of the papillary muscle marked in Fig. 6(b), again demonstrating the capacity of vacuum embedding to preserve suspended structures. We identified two hollow elliptical blood vessels within the papillary muscle (in the white rectangle area). The major axis of the elliptical blood vessels measured approximately $45.5\ \mu\text{m}$, the minor axis measured approximately $9.4\ \mu\text{m}$, and the thickness of the vascular wall was approximately $1.9\ \mu\text{m}$, which was consistent with the size of venules [27]. High-quality imaging and cutting enabled us to reconstruct the data in 3D and analyze the type and branch relationship of blood vessels. We reconstructed 3D venules through the pointed black holes [Fig. 6(e)] from 500 consecutive images; Fig. 6(f) illustrates the result. We observed that each venule was divided into two branches that passed through two cavities; therefore, the two venules were from the same branch. This finding may indicate that venules supply oxygen and nutrients to papillary muscles and dispose of generated carbon dioxide and waste.

4. Conclusion

This study presented an efficient and effective method to prepare a high-filled agarose-embedded whole-heart sample for thin tissue sectioning and organ-wide imaging. This method implemented a new vacuum-assisted embedding instrument. We determined the optimized processing parameters (vacuum pressure: $-60\ \text{kPa}$, vacuum time: 60 minutes), which achieved a higher fill factor (0.94) for the whole-heart sample compared with that achieved using the natural filling method (0.36). In addition, we compared the vibratome cutting effect using varying concentrations of agarose and determined that 6% agarose enabled the thinnest cutting of a complete $5\text{-}\mu\text{m}$ cardiac slice. To demonstrate the superiority of the new method, we subsequently implemented whole-heart imaging using a vibratome-integrated fMOST system. The imaging results indicated that even the hanging structures (i.e., the papillary muscle) were well-preserved, allowing for the tracing and reconstruction of the venules. The high-quality cutting and high-resolution imaging enabled us to identify and quantify fine structures, such as sarcomeres and vascular walls. These results established the potential of the vacuum-assisted embedding method for tissue sectioning and organ-wide imaging, particularly for cavity-containing tissues.

Funding. STI2030–Major Projects (2021ZD0204402); National Natural Science Foundation of China (82102235).

Acknowledgments. We thank the colleagues of the MOST group from the Britton Chance Center for Biomedical Photonics for their assistance.

Disclosures. J. Chen, Y. Li, R. Xie, J. Yuan, and Q. Luo have filed patent applications based on this research.

Data availability. Data underlying the results presented in this paper are not publicly available at this time but may be obtained from the authors upon reasonable request.

Supplemental document. See [Supplement 1](#) for supporting content.

References

1. K. R. Chien, I. J. Domian, and K. K. Parker, "Cardiogenesis and the complex biology of regenerative cardiovascular medicine," *Science* **322**(5907), 1494–1497 (2008).
2. X. Yang, T. Jiang, L. Liu, X. Zhao, X. Yu, M. Yang, G. Liu, and Q. Luo, "Observing single cells in whole organs with optical imaging," *J. Innov. Opt. Health Sci.* **16**(01), 2230011 (2023).
3. M. J. Suter, S. K. Nadkarni, G. Weisz, A. Tanaka, F. A. Jaffer, B. E. Bouma, and G. J. Tearney, "Intravascular optical imaging technology for investigating the coronary artery," *JACC Cardiovasc Imaging* **4**(9), 1022–1039 (2011).
4. I. Nehrhoff, D. Bocancea, J. Vaquero, J. J. Vaquero, J. Ripoll, M. Desco, and M. V. Gómez-Gaviro, "3D imaging in CUBIC-cleared mouse heart tissue: going deeper," *Biomed. Opt. Express* **7**(9), 3716–3720 (2016).
5. M. V. Gómez-Gaviro, D. Sanderson, J. Ripoll, and M. Desco, "Biomedical applications of tissue clearing and three-dimensional imaging in health and disease," *iScience* **23**(8), 101432 (2020).
6. C. Olianti, F. Giardini, E. Lazzeri, I. Costantini, L. Silvestri, R. Coppini, E. Cerbai, F. S. Pavone, and L. Sacconi, "Optical clearing in cardiac imaging: A comparative study," *Prog. Biophys. Mol. Biol.* **168**, 10–17 (2022).

7. K. R. Weiss, F. F. Voigt, D. P. Shepherd, and J. Huisken, "Tutorial: practical considerations for tissue clearing and imaging," *Nat. Protoc.* **16**(6), 2732–2748 (2021).
8. H. Kolesová, V. Olejníčková, A. Kvasilová, M. Gregorovičová, and D. Sedmera, "Tissue clearing and imaging methods for cardiovascular development," *iScience* **24**(4), 102387 (2021).
9. J. Chen, G. Liu, W. Sun, Y. Zheng, J. Jin, S. Chen, J. Yuan, H. Gong, Q. Luo, and X. Yang, "Three-dimensional visualization of heart-wide myocardial architecture and vascular network simultaneously at single-cell resolution," *Front. Cardiovasc. Med.* **9**, 945198 (2022).
10. J. Tang, H. Zhu, X. Tian, H. Wang, S. Liu, K. Liu, H. Zhao, L. He, X. Huang, Z. Feng, Z. Ding, B. Long, Y. Yan, N. Smart, H. Gong, Q. Luo, and B. Zhou, "Extension of endocardium-derived vessels generate coronary arteries in neonates," *Circ. Res.* **130**(3), 352–365 (2022).
11. S. Achanta, J. Gorky, C. Leung, A. Moss, S. Robbins, L. Eisenman, J. Chen, S. Tappan, M. Heal, N. Farahani, T. Huffman, S. England, Z. Cheng, R. Vadigepalli, and J. S. Schwaber, "A comprehensive integrated anatomical and molecular atlas of rat intrinsic cardiac nervous system," *iScience* **23**(6), 101140 (2020).
12. M. Brown, R. Reed, and R. Henry, "Effects of dehydration mediums and temperature on total dehydration time and tissue shrinkage," *J. Int. Soc. Plastination* **17**, 28–33 (2002).
13. J. J. Kelly, J. R. Ewen, S. L. Bernard, R. W. Glenn, and C. H. Barlow, "Regional blood flow measurements from fluorescent microsphere images using an Imaging CryoMicrotome," *Rev. Sci. Instrum.* **71**(1), 228–234 (2000).
14. M. Ranji, M. M. Motlagh, F. Salehpour, R. Sepehr, J. S. Heisner, R. K. Dash, and A. K. S. Camara, "Optical cryoimaging reveals a heterogeneous distribution of mitochondrial redox state in ex vivo guinea pig hearts and its alteration during ischemia and reperfusion," *IEEE J. Transl. Eng. Health Med.* **4**, 1 (2016).
15. L. Deng, J. Chen, and Y. Li, *et al.*, "Cryo-fluorescence micro-optical sectioning tomography for volumetric imaging of various whole organs with subcellular resolution," *iScience* **25**(8), 104805 (2022).
16. H. Wu, X. Yang, S. Chen, L. Zhang, B. Long, C. Tan, J. Yuan, and H. Gong, "On-line optical clearing method for whole-brain imaging in mice," *Biomed. Opt. Express* **10**(5), 2612–2622 (2019).
17. Y. Li, Z. Ding, L. Deng, G. Fan, Q. Zhang, H. Gong, A. Li, J. Yuan, and J. Chen, "Precision vibratome for high-speed ultrathin biotissue cutting and organ-wide imaging," *iScience* **24**(9), 103016 (2021).
18. E. Fernández, D. López, C. Mijangos, M. Duskova-Smrckova, M. Ilavsky, and K. Dusek, "Rheological and thermal properties of agarose aqueous solutions and hydrogels," *J. Polym. Sci. B Polym. Phys.* **46**(3), 322–328 (2008).
19. S. He, Q. Wen, C. O'Shea, R. Mu-u-min, K. Kou, A. Grassam-Rowe, Y. Liu, Z. Fan, X. Tan, X. Ou, P. Camelliti, D. Pavlovic, and M. Lei, "A protocol for transverse cardiac slicing and optical mapping in murine heart," *Front. Physiol.* **10**, 755 (2019).
20. Q. Zhong, A. Li, R. Jin, D. Zhang, X. Li, X. Jia, Z. Ding, P. Luo, C. Zhou, C. Jiang, Z. Feng, Z. Zhang, H. Gong, J. Yuan, and Q. Luo, "High-definition imaging using line-illumination modulation microscopy," *Nat. Methods* **18**(3), 309–315 (2021).
21. S. Miller, "Methods for computing the boiling temperature of water at varying pressures," *Bull. Amer. Meteorol. Soc.* **98**(7), 1485–1491 (2017).
22. X. Xia, Y. Yao, J. Liang, S. Fang, Z. Yang, and D. Cui, "Evaluation of focus measures for the autofocus of line scan cameras," *Optik* **127**(19), 7762–7775 (2016).
23. E. Peli, "Contrast in complex images," *J. Opt. Soc. Am. A* **7**(10), 2032–2040 (1990).
24. M. Mesradi, A. Genoux, V. Cuplov, D. AbiHaidar, S. Jan, I. Buvat, and F. Pain, "Experimental and analytical comparative study of optical coefficient of fresh and frozen rat tissues," *J. Biomed. Opt.* **18**(11), 117010 (2013).
25. P. P. Sengupta, J. Korinek, M. Belohlavek, J. Narula, M. A. Vannan, A. Jahangir, and B. K. Khandheria, "Left ventricular structure and function: Basic science for cardiac imaging," *J. Am. Coll. Cardiol.* **48**(10), 1988–2001 (2006).
26. Y. Kanzaki, F. Terasaki, M. Okabe, S. Fujita, T. Katashima, K. Otsuka, and N. Ishizaka, "Three-dimensional architecture of cardiomyocytes and connective tissue in human heart revealed by scanning electron microscopy," *Circulation* **122**(19), 1973–1974 (2010).
27. M. Bert, L. Sabrina, D. Marco, R. Markus, S. Georg, D. Hans, G. Marco, P. Franz, D. Christian, and W. Timm, "High-resolution tomographic imaging of microvessels," *Proc. SPIE* **7078**, 70780B (2008).